Residual thermal stresses in injection molded products

Residual Thermal Stresses in Injection Molded Products

W. F. ZOETELIEF,* L. F. A. DOUVEN,* *and* A. J. INGEN HOUSZ**

Eindhoven University of Technology
Faculty of Mechanical Engineering
Section of Experimental and Computational Mechanics
5600 MB Eindhoven, The Netherlands

Nonisothermal flow of a polymer melt in a cold mold cavity introduces stresses that are partly frozen-in during solidification. Flow-induced stresses cause anisotropy of mechanical, thermal, and optical properties, while the residual thermal stresses induce warpage and stress-cracking. In this study, the influence of the holding stage on the residual thermal stress distribution is investigated. Calculations with a linear viscoelastic constitutive law are compared with experimental results obtained with the layer removal method for specimens of polystyrene (PS) and acrylonitrile butadiene-styrene (ABS). In contrast to slabs cooled at ambient pressures, which show the well-known tensile stresses in the core and compressive stresses at the surfaces, during the holding stage in injection molding, when extra molten polymer is added to the mold to compensate for the shrinkage, tensile stresses may develop at the surface, induced by the pressure during solidification.

INTRODUCTION

Injection molding is a flexible production technique for the manufacturing of polymer products. During processing, the polymer experiences a complex deformation and temperature history that affects the final properties of the product. Nowadays, the demands on high dimensional stability and close dimensional tolerances require knowledge of the mechanisms that affect the properties.

Residual stresses influence the properties of injection molded products (1–4). These stresses mainly originate from two sources. First, viscoelastic flow of the melt during the filling and post-filling stage of the process causes frozen-in *flow-induced stresses*. These stresses correspond with the orientation of the macromolecules. Second, differential shrinkage during cooling, both inside the mold and after demolding, causes the *residual thermal stresses*. In absolute value, the flow-induced stresses are an order of magnitude smaller than the thermal stresses. However, they induce anisotropy of several properties, because of the different orientations in the direction parallel and perpendicular to the flow direction. On the other hand, the residual stresses cause warpage and may induce environmental stress-cracking.

In the development of numerical codes for simulating injection molding, attention nowadays focuses on the prediction of product properties. This calls for the simulation of the complete injection molding cycle, instead of only analyzing one specific molding stage like injection. For example, calculation of the flow-induced stresses in the filling stage (5) has been extended to the post-filling stage (3, 4) because birefringence measurements have shown that during packing and holding, large orientations may develop (6, 7). Moreover, predictions of residual stresses in injection molded products show large deviations from residual stresses in freely quenched samples (1, 2, 8). The latter experiment results in a parabolic shaped gapwise stress profile, since the rapid inhomogeneous cooling of the surfaces forms a rigid shell, which prevents free contraction of the core material (9–11). This results in compressive stresses near the surface equilibrated by tensile stresses in the core, while in the case of injection molding, tensile stresses in the region close to the surface are often found (1).

Calculated gapwise thermal stress distributions are compared here with experimental results. The calculations involve the complete modeling of the injection molding process, since temperature and pressure change in every stage of the cycle.

First, the development of residual stresses in an injection molded product is explained by a schematic example. This example may help in defining the proper boundary conditions for the thermal stress cal-

* Present address: Philips Research Laboratories, Prof. Holstlaan 4, 5656 AA Eindhoven, The Netherlands.

** University of Twente, Department of Mechanical Engineering, P.O. Box 217, 7500 AE Enschede, The Netherlands.

culations. Next, the thermal stress problem (TSP) will be derived using a linear thermo-viscoelastic constitutive law; a strategy for the numerical solution is given.

For the determination of the thermal stresses, the layer removal method (12) is used. The expressions that relate the measured curvature to the stresses as used in the layer removal method will be extended to take warpage into account, due to uneven cooling of the mold walls.

Finally, the solution of the TSP is applied on two problems with different holding situations, and predictions are compared with experimental results. The possible influence of flow-induced anisotropy due to orientation on the thermal stresses is not considered.

AN ILLUSTRATION OF STRESS DEVELOPMENT

The principles of the development of residual thermal stresses will be illustrated by means of a schematic representation of an injection molding experiment, analogous to the example of Struik (9, 10) for the free quench experiment. Cooling is idealized in five steps in which also the pressure varies as a function of time (see *Fig. 1*). As the cooling front moves inwards, the temperature drops from $T_h > T_g$ to $T_l < T_g$, where T_g is the glass transition temperature. It is assumed that the material behaves as an ideal fluid when $T > T_g$, thus $\sigma = -p\mathbf{I}$, and linear elastic when $T < T_g$.

When at $t = t_0$ the mold is completely filled, the residual thermal stresses develop as follows:

- $t = t_0$: Full mold; the temperature is homogeneous and equals T_h; the pressure is zero; and the material is free of stresses.
- $t = t_1$: Contraction of the outer layers is hindered by the no-slip condition at the mold walls. A small tensile stress $\sigma_{xx}(z)$ is introduced in the solidified outer shells.
- $t = t_2$: A holding pressure p acts on the melt resulting in a compressive stress $\sigma = -p_h$, compressing the rigid shell. As a result, the stress in these layers is decreased by $\Delta\sigma = \nu p_h/(1 - \nu)$ (assuming that all displacements in the x-direction in the shell are suppressed), with ν Poisson's ratio.
- $t = t_3$: During the holding stage the pressure remains constant, while a small layer of the material solidifies during the time interval $[t_2, t_3]$. Contraction of the newly cooled material decreases the compressive stress in the surface layers.
- $t = t_4$: The pressure is set to zero and the stress in the melt disappears. The stresses in the rigid shell increase with $\Delta\sigma$.
- $t = t_5$: Finally, the product is released from the mold. Further cooling is now similar to a free quench. This results in tensile stresses in the core that are in equilibrium with the stresses in the outer layers.

Instead of compressive surface stresses in the case of a free quench experiment, tensile stresses occur at

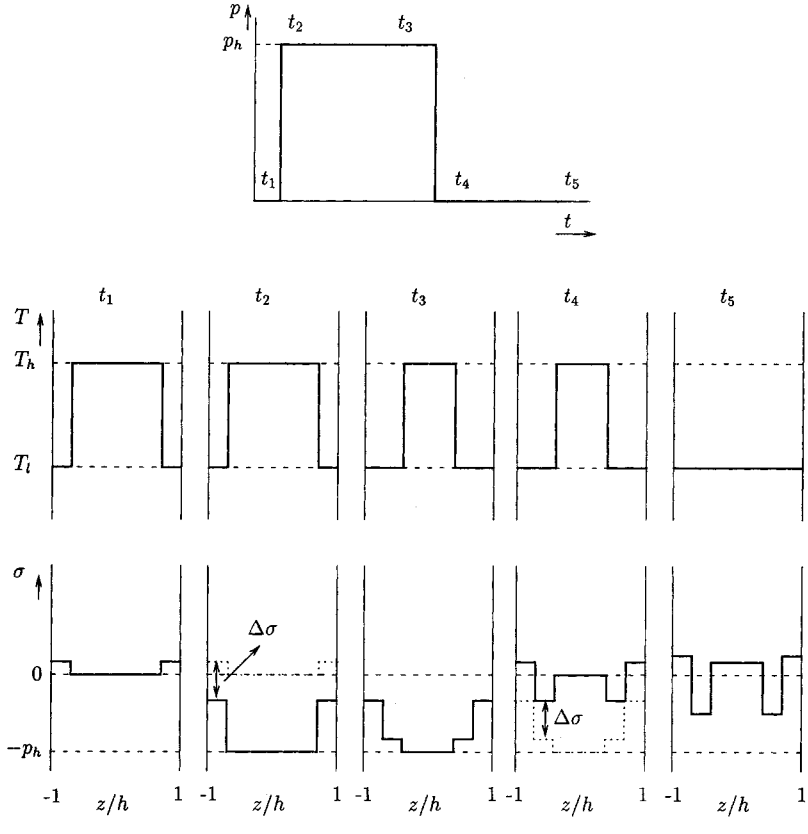

Fig. 1. Residual stress development in injection molded products.

the surface of the sheet. These tensile stresses are ~10 MPa and depend mainly on the magnitude and duration of the holding pressure. The residual thermal stresses are induced by a hydrostatic pressure in combination with rapid cooling, so the stresses in the x-direction must equal those in the y-direction (see *Fig. 2* for definitions).

CALCULATIONS

As argued above, the calculation of the residual thermal stresses requires the simulation of the complete injection molding cycle. The governing equations that describe the process consist of a set of balance equations and constitutive relations. The set of equations can be simplified considerably using the thin-film approximation. In this way the geometrical characteristics found in many injection molded products, i.e., thin and flat or weakly curved shapes, are brought into account. Detailed information with relation to the solution of this set of equations can be found in the literature (1, 2, 4, 13, 14).

Basic Assumptions

1. All the assumptions employed using the thin-film approximation are valid. The temperature and pressure fields that are the output of the simulation of mold filling, holding, and packing are used as input for the calculation of the thermal stresses. The stress component in the thickness direction of the product σ_{zz} equals minus the melt pressure (i.e. injection, holding, and packing pressure) for as long as the temperature in the midplane of the cavity T^* is above T_g.
2. As long as the melt pressure is non-zero in a point of the midplane Γ_0, the material sticks to the mold walls in this point. So global displacements are zero. The only non-zero strain component is ϵ_{zz}.
3. If the pressure drops to zero in a point of Γ_0, the material is permitted to lose contact from the mold walls.
4. The gap between product surface and mold wall that may develop if the pressure is zero is assumed not to influence heat transport.
5. There is no interaction between the flow-induced stresses and the thermally induced stresses.
6. Bending is taken into account only after the product is ejected from the mold.
7. Mold elasticity is taken into account by taking $\partial h/\partial t = C_m \partial p/\partial t$, with C_m the mold compliance (1, 3), h the gapwidth, and p the cavity pressure.

Formulation of the Thermal Stress Problem

Summarized, the thermal stress problem (TSP) is defined as

Given:

a temperature field $T(\vec{x}, t)$,
a pressure field $p(\vec{x}, t)$,
a boundary displacement field $\vec{u}^0(\vec{x}, t)$,
and a boundary load $\vec{f}^0(\vec{x}, t)$,

find:

the displacement field $\vec{u}(\vec{x}, t)$

such that:

the balance equations

$$\vec{\nabla} \cdot \boldsymbol{\sigma}^c = \vec{0}, \quad \boldsymbol{\sigma} = \boldsymbol{\sigma}^c \tag{1}$$

constitutive behavior (linear thermo-viscoelasticity)

$$\boldsymbol{\sigma} = p^h \mathbf{I} + \boldsymbol{\sigma}^d \tag{2}$$

$$\boldsymbol{\sigma}^d = \sum_{i=1}^{m} 2 \int_0^t G_i e^{-(\xi(t)-\xi(\tau))/\theta_i} \dot{\boldsymbol{\epsilon}}^d \, d\tau, \quad \xi(\tau) = \int_0^\tau \frac{1}{a_T} \, ds \tag{3}$$

$$p^h = -\frac{1}{3} tr(\boldsymbol{\sigma}) = \int_0^t \left(\frac{\alpha}{\kappa} \dot{T} - \frac{1}{\kappa} tr(\dot{\boldsymbol{\epsilon}}) \right) d\tau \tag{4}$$

and boundary conditions

$$\vec{u} = \vec{u}^0 = \vec{0} \tag{5}$$

$$\vec{n} \cdot \boldsymbol{\sigma} = \vec{f}^0 = \vec{0} \tag{6}$$

are satisfied, applying all assumptions mentioned above.

In equations above, $\boldsymbol{\sigma}$ is the Cauchy stress tensor, $\boldsymbol{\epsilon}$ the linear strain tensor, G_i and θ_i the shear modulus and relaxation time of the i-th mode of the multi-mode Maxwell model, a_T the shift factor of the time-temperature superposition principle, α is the temperature dependent thermal volume expansion coefficient, κ the compressibility coefficient, T the temperature, p^h the hydrostatic pressure and $\mathbf{I}$ the unit tensor. The superscripts c, d refer to the conjugation and the deviatoric part of a second order tensor resp. Consider-

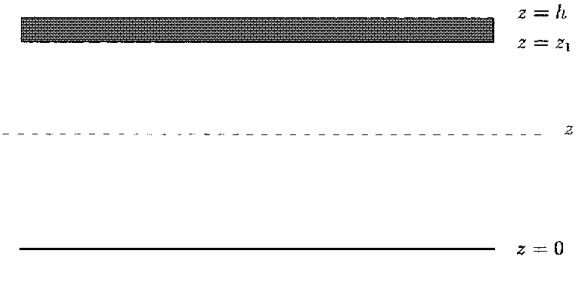

Fig. 2. Rectangular section of flat specimen.

ing their definitions, α and κ can be evaluated from the pvT-data.

For comparison, linear thermo-elastic constitutive behavior is also modeled, expressed by

$$\boldsymbol{\sigma}^d = 2G_{el}\dot{\boldsymbol{\epsilon}}^d, \tag{7}$$

with G_{el} the elastic shear modulus.

Note that in the balance of momentum equation (*Eq 1*), the volume and inertial forces are neglected. In the formulation it is assumed that the material behaves thermorheologically simply (15). The normal vector $\vec{n}$ is perpendicular to the midplane, thus $\vec{n} = \vec{e}_z$. The boundary of the product is split into two parts. On one part, $\Gamma_k(t)$, the kinematic boundary condition (5) applies (free quench), whereas on the other part, $\Gamma_d(t)$, the dynamic boundary condition (6) applies (constrained quench).

Numerical Solution of the Thermal Stress Problem

For the numerical solution of the TSP, the linear thermo-viscoelastic constitutive equation is written in an incremental form (see (1, 2, 4)). In this way, the stress state at time t_{n+1} can be evaluated using the completely determined stress state at time t_n together with the pressure and temperature history at t_{n+1}. Further details can be found in **Appendix A.**

Boundary Conditions

Four different situations must be considered in each point of the midsurface Γ_0, which can be derived from the schematic example:

1. The pressure is non-zero and the temperature in the midsurface, T^*, is still above T_g:

$$p(=-\sigma_{zz}) \geq 0, \quad T^* \geq T_g(p) \tag{8}$$

2. The pressure is non-zero and the temperature in the mid surface, T^*, is below T_g:

$$p \geq 0, \quad T^* < T_g(p) \tag{9}$$

3. The pressure is zero, but the product is still in the mold:

$$p = 0, \quad t < t_{de} \tag{10}$$

4. The pressure is zero, and the product is ejected:

$$p = 0, \quad t \geq t_{de} \tag{11}$$

These four cases are now analyzed in somewhat more detail.

1. Constrained Quench With Fluid Core

All strain components are zero for $z \in [-h/2, h/2]$, except ϵ_{zz} must obey $\int_{-h/2}^{h/2}\epsilon_{zz}\,dz = 0$. When substituting $\Delta\epsilon = 0$ in *Equation A.12*, the non-zero stress components are given by:

$$\sigma_{zz} = -p, \tag{12}$$

$$\sigma_{xx} = \sigma_{yy} = \sigma_{xx}^{\cdot} + \frac{b}{a}(-p - \sigma_{zz}^{\cdot}), \tag{13}$$

where $\sigma^{\cdot}$, a, b are a result of the incremental formulation given in **Appendix A.**

2. Constrained Quench With Solid Core

Same as case one. Since σ_{zz} is not explicitly given, it has to be evaluated from the condition $\int_{-h/2}^{h/2}\epsilon_{zz}\,dz = 0$. With the aid of *Eq A.11*, this results in

$$\sigma_{zz} = \frac{\displaystyle\int_{-h/2}^{h/2}(\sigma^{\cdot}/a)dz}{\displaystyle\int_{-h/2}^{h/2}(1/a)\,dz}. \tag{14}$$

The other non-zero stress components are given by *Eq 13.*

3. Free Quench, in the Mold

The only zero strain components are the shear strains ϵ_{xz} and ϵ_{yz}, because bending is assumed to be prevented by the mold that envelops the product. The stress components are calculated by solving *Eq A.12.*

4. Free Quench, Demolded

All strain components may be non-zero and stresses are evaluated by means of *Eq A.12.*

It may be obvious that in cases 1 and 2, no calculation of the displacements is required, since they are prescribed by *Eq 5.* In cases 3 and 4, however, the displacement field is approximated by means of a finite element calculation, where the boundary condition in *Eq 6* applies. For this purpose, a shell element has been developed. With the displacement field thus obtained, the stresses can be calculated.

Element Formulation

For solving the displacement field for the cases 3 and 4, the spatial discretization is performed by using the finite element method. The displacement field is solved for each discrete time t_{n+1} using a shell element based on the Mindlin plate theory. Thus, transverse shear strains are not assumed to be zero [see ref 16, Ch. 6, and refs. 17 and 18]. The element is a four-node bilinear isoparametric element, having five degrees of freedom per node.

LAYER REMOVAL METHOD

Measurements of residual thermal stresses are frequently carried out with the layer removal method. This method is relatively easy to apply to flat specimens and gives information about the stress distribution in the gapwise direction. Treuting and Read developed this method for determining residual stresses in metal sheets. Isayev (13) provides a list of authors who successfully applied this method to polymers. The principle of the method is based on disturbing the stress-equilibrium in a rectangular specimen by removing thin layers of uniform thickness from one surface. After layer removal, the specimen will warp to the

shape of a circular arc to establish stress-equilibrium. The residual stress distribution in the original sample can now be calculated using the measured curvature values.

Analysis of the Stress-Curvature Relation

In this analysis, the original relation of Treuting and Read (12) is modified. An initial curvature is introduced to take the initial warpage of the specimen in the case of asymmetric cooling into account. *Figure 2* shows a rectangular section of the specimen together with the coordinate system used. The x and y axes coincide with the directions of principal stress and the z axis with the thickness direction. The x-direction is also the flow direction. The boundary condition that is modified for stress-equilibrium is given by

$$M_x(h) = \int_0^h \sigma_x(z)\left(z - \frac{h}{2}\right)dz = M_{x_0} \qquad (15)$$

Where M_x is the bending moment, σ_x the stress, M_{x_0} the initial bending moment, z the coordinate in the thickness direction, and h the thickness of the specimen. The same relation will hold for the y direction when exchanging the subscripts x and y. With *Eq 15* as a boundary condition, the biaxial stress equation can be derived:

$$\sigma_x(z_1) = -\frac{E}{6(1-\nu^2)}\left\{z_1^2\left[\frac{d\kappa_x(z_1)}{dz_1} + \nu\frac{d\kappa_y(z_1)}{dz_1}\right]\right. \qquad (16)$$

$$+ 4z_1[\kappa_x(z_1) + \nu\kappa_y(z_1)] - h[\kappa_{x_0} + \nu\kappa_{y_0}]$$

$$\left. - 2\int_{z_1}^{h}[\kappa_x(z) + \nu\kappa_y(z)]dz\right\}$$

where z_1 is the remaining thickness, E is the Young's modulus, ν the Poisson's ratio, and κ_x, κ_y, κ_{x_0}, κ_{y_0} the (initial) curvatures in the x, y directions. The relation for $\sigma_y(z_1)$ can be derived by exchanging the x and y subscripts.

The general biaxial formulation can be simplified by assuming the stresses to be isotropic, i.e. $\sigma_x(z) = \sigma_y(z)$, leading to:

$$\sigma_x(z_1) = -\frac{E}{6(1-\nu)}$$

$$\cdot\left\{z_1^2\frac{d\kappa_x(z_1)}{dz_1} + 4z_1\kappa_x(z_1) - h\kappa_{x_0} - 2\int_{z_1}^{h}\kappa_x(z)dz\right\} \qquad (17)$$

The experimental work in this case is limited to measuring the curvature in one direction only.

Since molecular orientation is not taken into account, the residual stresses are assumed to be isotropic. Therefore *Eq 17* is justified.

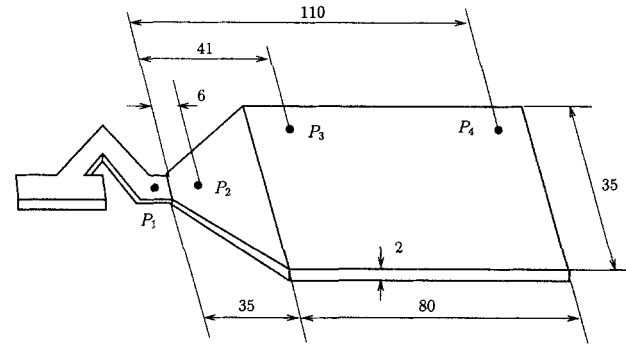

Fig. 3. Flat strip mold A (PS) (dimensions are in mm).

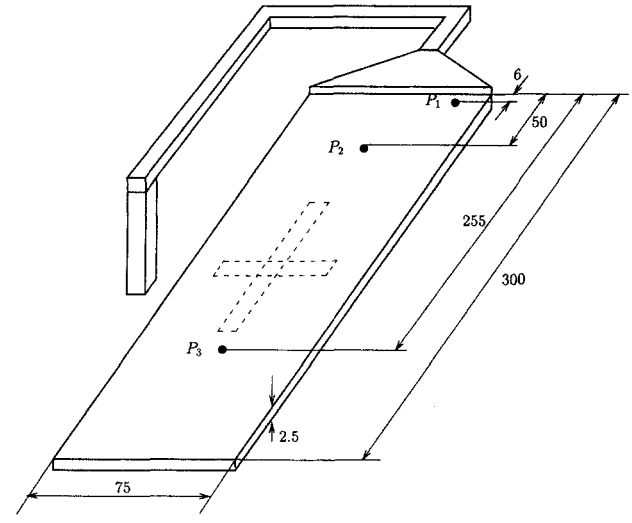

Fig. 4. Rectangular strip mold B (ABS) (dimensions are in mm).

RESULTS

In this section, results of the calculations are compared with experimental results for two different test specimens. Specimen A, shown in *Fig. 3*, is molded of polystyrene (PS, Styron 678E of Dow Chemical) at the Philips Plastics and Metalware Factories (2, 3, 19), indicated there as PS55. Specimen B is a rectangular strip (300 × 75 × 2.5 mm) molded of acrylonitrile-butadiene-styrene (ABS, Novodur P2X of Bayer) (see *Fig. 4*). Both molds were equipped with pressure transducers to monitor the place-dependent pressure in time. The positions of the transducers are shown in *Figs. 3* and *4* for specimen A and B, respectively. The main processing parameters are summarized in *Table 1*.

Table 1. Process Parameters.

		PS	ABS
T_{inj}	K	473	513
T_{wall}	K	328	325/321
Q	m³/s	$7.6 \cdot 10^{-6}$	$1.2 \cdot 10^{-5}$
p_{entry}	see *fig.*	6	13

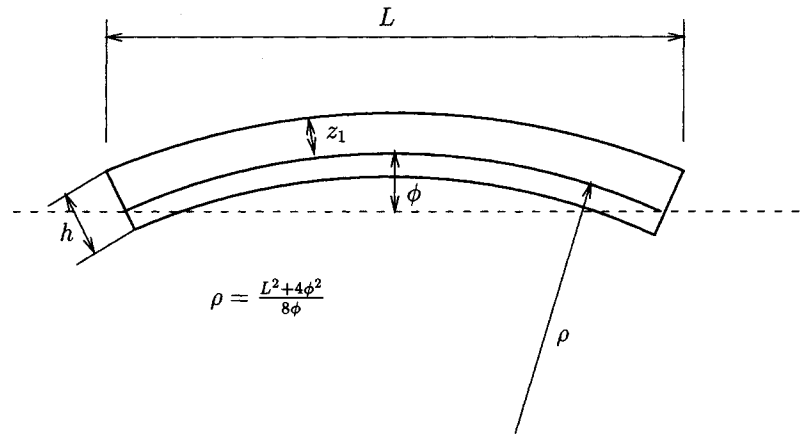

Fig. 5. Determination of curvature of a deformed bar.

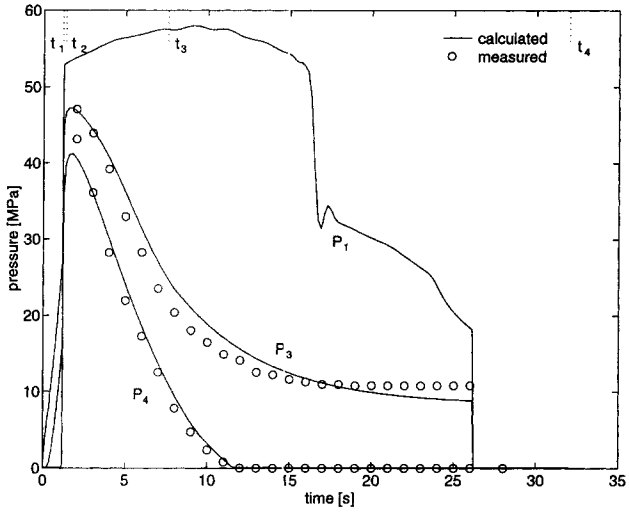

Fig. 6. Pressure history for specimen A (PS) at different locations along flowpath (t_1: end of filling, t_2: end of packing, t_3: end of holding, and t_4: after ejection).

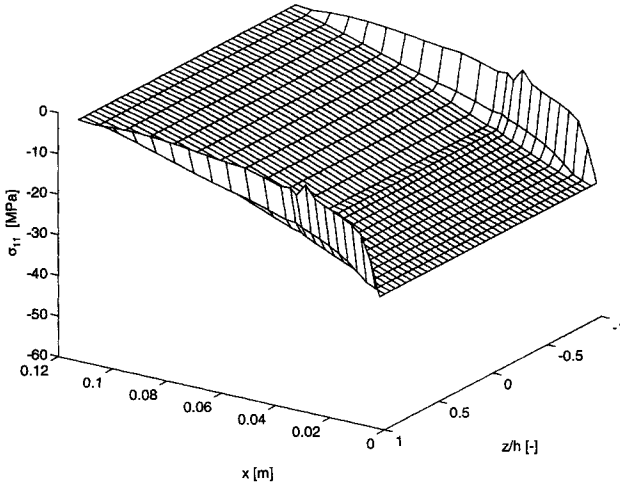

Fig. 7. Stress distribution specimen A (PS) at the end of filling (t_1 = 1.19s).

The procedure for measuring the residual stresses differ for the two specimens. For the specimens of mold B, bars of 100 × 5 mm were cut out in the flow direction (x-direction) and bars of 50 × 5 mm in the y-direction of the strip. By doing so, residual stresses in both directions can be determined. Because the mold cooling was asymmetrical, the procedure of layer removal is carried out for both surfaces. For the layer removal, a conventional milling machine with a 20 mm end-mill operating at 1400 rpm was used. These milling conditions gave reproducible results, although it is not known if extra stresses were introduced. For practical reasons, for every layer removal, a new bar was taken. During milling, the bars were held flat by double-sided adhesive tape. After removal of a layer the curvature $\kappa = 1/\rho$ was determined by measuring the deflection ϕ with an optical microscope (see *Fig. 5*). For further analysis, the curvature data are fitted by a high order polynomial function. For the measurement of the series A, Van Hastenberg *et al.* (19) modified our procedure to measure the stresses along the flowpath of a (flat) product.

The numerical simulations are carried out with a visco-elastic (see *Eq 3*) and a viscous-elastic [according to (7)] modeling of the shear modulus. In the latter model the modulus in the melt is neglected (equals zero), while the modulus in the solid is equal to the elastic shear modulus G_{el}, whereas in the visco-elastic representation the multi-mode Maxwell model is used. The material parameters used in the calculations are listed in *Table 4* for both materials. In the calculations the runner section is not taken into account. The measured pressure history at position P_1 (see *Figs. 3* and *4*), representing the gate, is prescribed during packing, holding, and cooling, and thus can be considered as the holding parameter.

Results for Specimen A (PS)

The calculated and measured pressure histories are shown in *Fig. 6*. The labels P_1, P_3, and P_4 refer to the positions of the pressure transducers in *Fig. 3*. *Figures 7* through *10* show, with the visco-elastic model calculated gapwise, residual stress profiles as a function of the flow-path x for four different timesteps: at the end of filling, at the end of packing, at the end of holding, and after part ejection. The gapwise stress

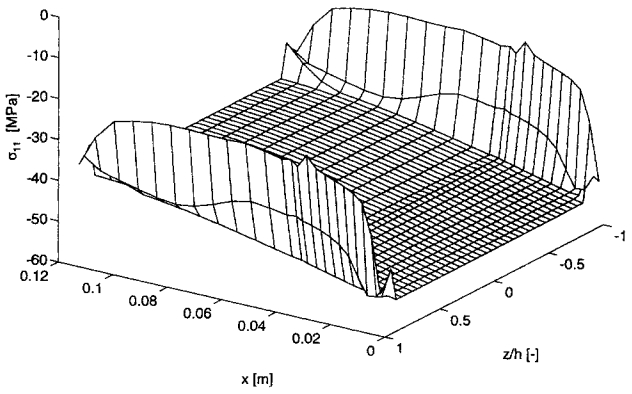

Fig. 8. Stress distribution specimen A (PS) at the end of packing (t_2 = 1.25s).

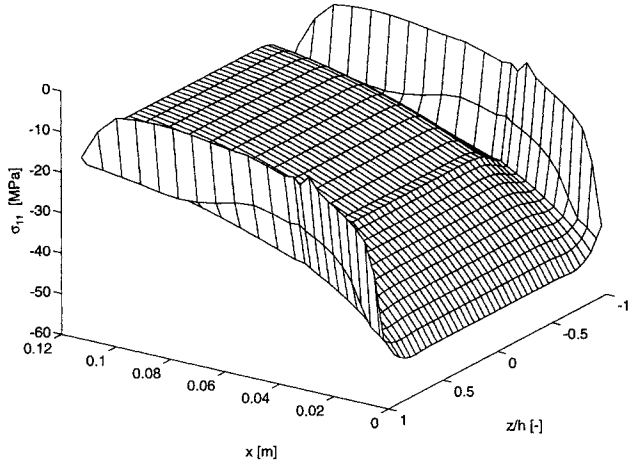

Fig. 9. Stress distribution specimen A (PS) at the end of holding (t_3 = 7.57s).

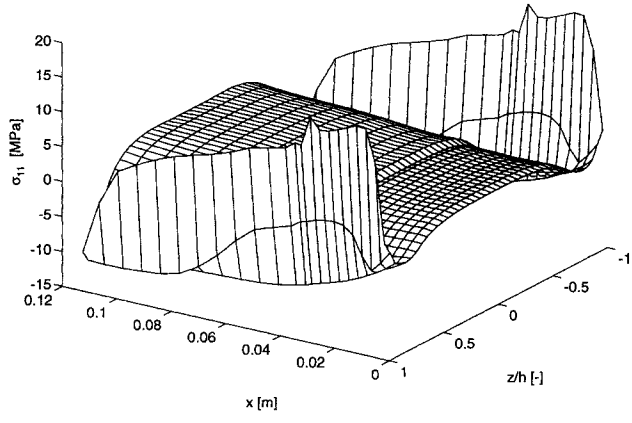

Fig. 10. Stress distribution specimen A (PS) after ejection (t_4 = 32.0s).

profiles at a location halfway the strip at the end of the four stages is plotted in *Figs. 11a* and *b* for the visco-elastic and the viscous-elastic model, respectively. The stress development shown in these *Figures* is in qualitative agreement with the schematic example given in *Fig. 1.*

In *Fig. 12* the experimental and calculated stress profiles are compared. In addition to the results of the visco-elastic calculation (*Fig. 11a*, curve 4), the results of a viscous-elastic calculation (*Fig. 11b*, curve 4) are plotted. *Figure 12* shows that all three stress profiles have the same shape, tensile stresses at the surface, followed by a region with compressive stresses more inward, and again tensile stresses in the core of the sample. The results of the visco-elastic calculation show a slightly better agreement with the experimental results than the viscous-elastic simulation. The position of the minima is better predicted, as well as the value of the tensile stresses at the surface. However, the compressive stresses near the surface are overpredicted.

Results for Specimen B (ABS)

Figure 13 shows the calculated and measured pressure history at different locations along the flow path. The labels P_1, P_2, and P_3 refer to the positions of the pressure transducers in *Fig. 4.*

Figures 14a and *b* show the final gapwise stress distributions as a function of the flowpath x for the visco-elastic and viscous-elastic models, respectively. Both models show qualitatively the same result as for PS. The final stress distribution of the visco-elastic case shows that for the part of the product at the end of the flowpath, the tensile stress in the core is somewhat lower than in a region closer to the gate. The reason for this behavior is that for a large part of the product, the pressure dropped to atmospheric levels while the material was still not solidified. This induces a free quench situation in the mold for that part of the product, while the other part experiences a constrained quench with a fluid core.

Figure 15 shows the measured curvature values for the bars removed from the strip in the x-direction and the y-direction. The consequences of the asymmetrical cooling can be seen clearly in this *Figure.* Despite the high order of the polynomial function used for fitting, not all details in the region close to the surfaces, viz., an underestimation of the derivative of the curvature, are captured. As a consequence, the stresses near the walls are somewhat underestimated. Finally, in *Fig. 16,* the calculated stress profiles at a position between P_2 and P_3 are compared with the experimental values. Again, there is a qualitative agreement between the measured and the calculated results. Apparently, the experimental results for the x and y directions coincide. Moreover, the calculated stresses in the in-plane direction are the same, since no anisotropy is taken into account. In absolute value, the visco-elastic calculations agree quantitatively better with the experiments.

From this *Figure,* it can also be seen that the imbalance in the cooling of the product has seemingly a slight effect on the symmetry of the stress profile. However, this asymmetry causes a small but unwanted warpage of the product.

CONCLUSIONS

The residual stress development in injection molded products was investigated numerically and experi-

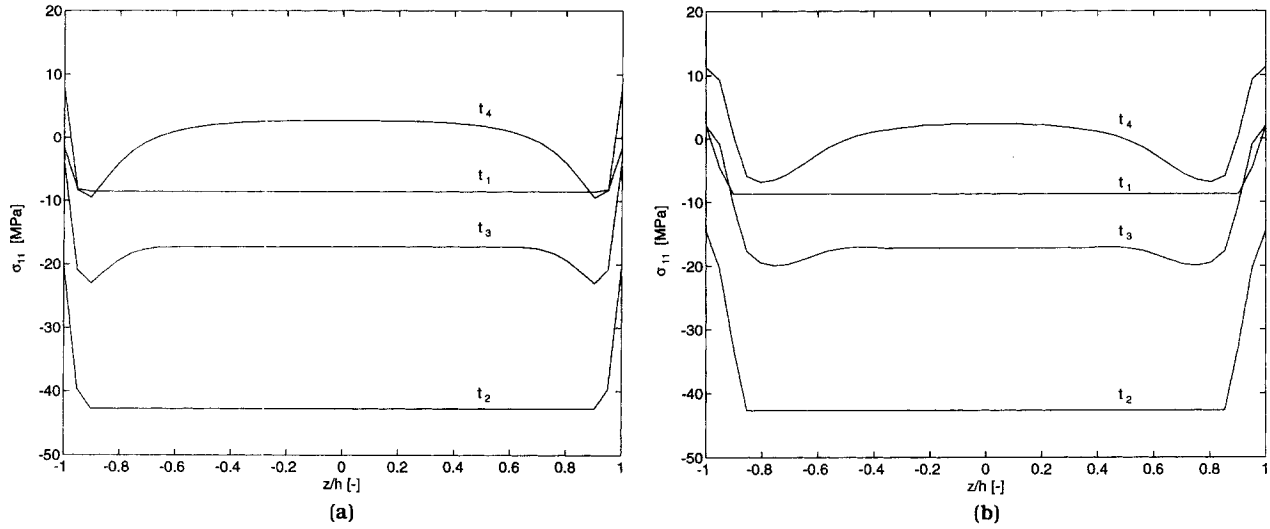

Fig. 11. Gapwise stress distribution halfway the flowpath for specimen A (PS), visco-elastic (a) and viscous-elastic calculation (b) (t_1: end of filling, t_2: end of packing, t_3: end of holding, and t_4: after ejection).

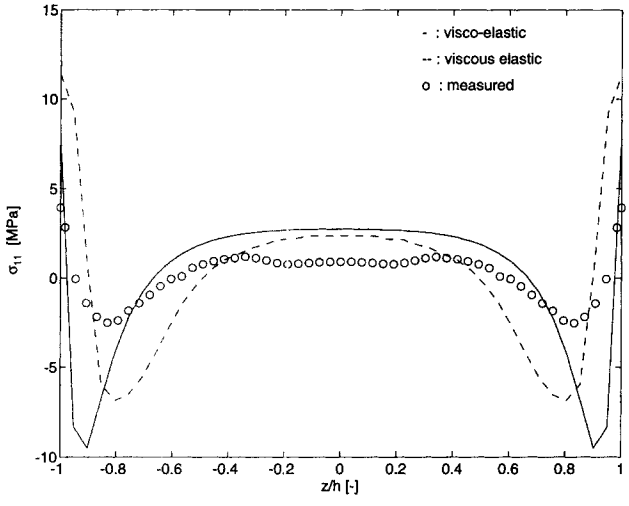

Fig. 12. Gapwise stress distribution specimen A (PS).

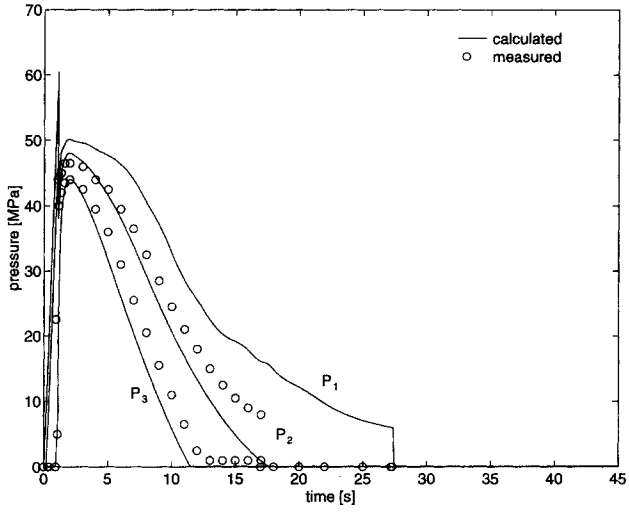

Fig. 13. Pressure history for specimen B (ABS) at different locations along flowpath.

mentally for specimens of two different amorphous polymers.

Calculations show that considerable tensile stress at the surface of injection molded products arises during the holding and packing stage. This tensile stress is caused by the high mold pressure that occurs during the process. Therefore, it is better to speak of the development of pressure-induced residual stresses than of thermally induced stresses. Since the pressure is a main factor in the development of the residual stress state, it is important to predict the pressure decay during the holding and cooling stages as accurately as possible. Introducing mold elasticity appeared necessary to get better agreement between calculations and measurements in this part of the process.

Calculations with the visco-elastic model agree slightly better with the experimental results than those obtained from the viscous-elastic model. However, the model gives a good qualitative description of the residual stress development at considerable less computing costs.

In the analysis, the influence of the orientation on the material properties has not been taken into account, as well as the influence of the flow-induced stresses. Until now, it is not known if the flow-induced stresses may simply be added to the pressure-induced and thermally induced stresses to form the final stress distribution. Of course, via the flow-induced stresses, a measure of molecular orientation can be derived that can be included in the calculation to take anisotropy of material properties into account. Assuming that the residual stress state is isotropic, is then no longer valid. However, from the measurements in both the flow direction and the direction normal to the flow, no difference could be observed between the two so-obtained stress distributions. This confirms the expectation that the tensile stresses are solely induced by the mold pressure.

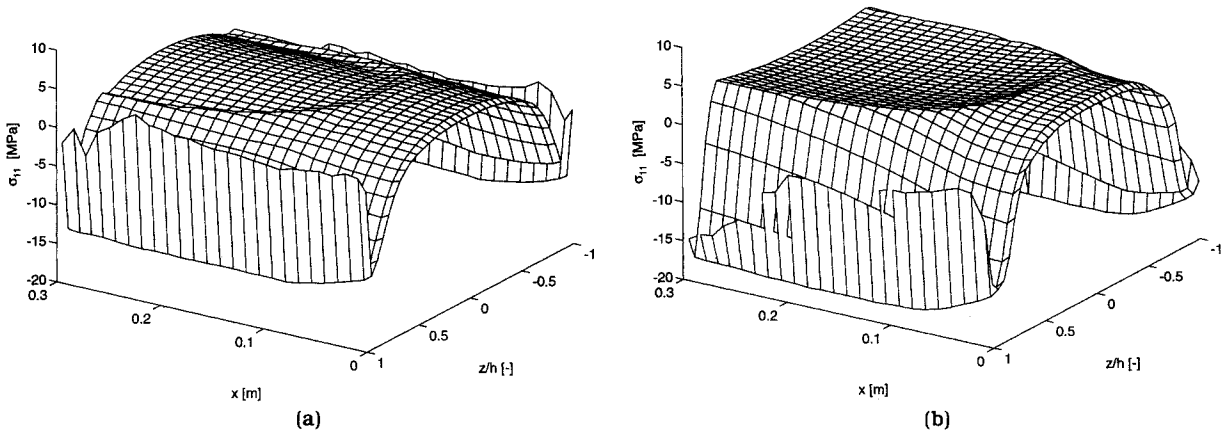

Fig. 14. Stress distribution specimen B (ABS) after ejection (t = 45.0s), visco-elastic (a) and viscous-elastic calculation (b).

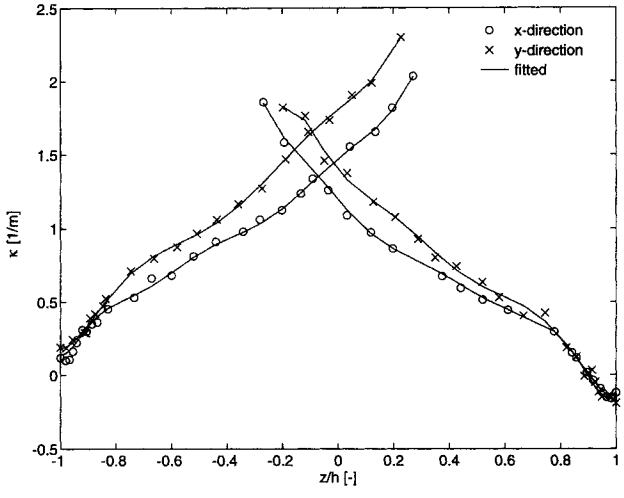

Fig. 15. Experimental curvature data (symbols) and polynomial fit (solid line) for specimen B (ABS).

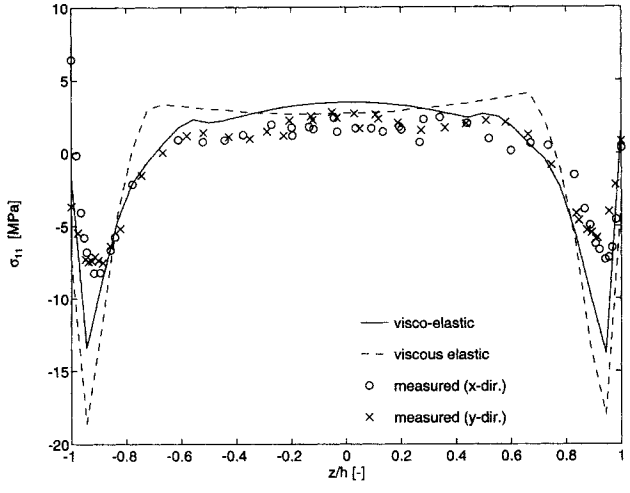

Fig. 16. Gapwise stress distribution specimen B (ABS).

APPENDIX A: NUMERICAL SOLUTION OF THE THERMAL STRESS PROBLEM

Incremental Formulation

For the numerical solution of the TSP, the linear thermo-viscoelastic constitutive equation is written in an incremental form [see (1)]. The Cauchy stress tensor as expressed by *Eqs 2* through *4* at time $t = t_n$ reads

$$\boldsymbol{\sigma} = p_n^h \mathbf{I} + \sum_{i=1}^{m} \boldsymbol{\sigma}_{i_n}^d, \tag{A.1}$$

$$p_n^h = \int_0^{t_n} \left(\frac{\alpha}{\kappa} \dot{T} - \frac{1}{\kappa} tr(\dot{\boldsymbol{\epsilon}}) \right) d\tau, \tag{A.2}$$

$$\boldsymbol{\sigma}_{i_n}^d = 2 \int_0^{t_n} G_i e^{-(\xi_n - \xi(\tau))/\theta_i} \dot{\boldsymbol{\epsilon}}^d \, d\tau. \tag{A.3}$$

Note that a subscript n indicates evaluation at time t_n. The state at t_n is completely determined. Next the stress state at t_{n+1} can be evaluated when the temperature and strain fields are solved for this time. An incremental formulation for the stresses is derived where only values at the previous time t_n need to be known. The following incremental variables are introduced

$$\Delta\xi_{n+1} = \xi_{n+1} - \xi_n, \quad \Delta T_{n+1} = T_{n+1} - T_n, \tag{A.4}$$

$$\Delta\boldsymbol{\epsilon}_{n+1} = \boldsymbol{\epsilon}_{n+1} - \boldsymbol{\epsilon}_n .$$

It is assumed that $\boldsymbol{\epsilon}$ and T vary linearly between two discrete times, implying that $\dot{\boldsymbol{\epsilon}}$ and $\dot{T}$ are constant over each time increment, thus yielding

$$\dot{\boldsymbol{\epsilon}} = \frac{\Delta\boldsymbol{\epsilon}_{n+1}}{\Delta t_{n+1}}, \quad \dot{T} = \frac{\Delta T_{n+1}}{\Delta t_{n+1}} \quad \text{for} \quad t \in [t_n, t_{n+1}]. \tag{A.5}$$

After extensive rewriting of *Eq A.1* for $t = t_{n+1}$, the following expression is derived for $\boldsymbol{\sigma}_{n+1}$

$$\boldsymbol{\sigma}_{n+1} = \boldsymbol{\sigma}^{\cdot} + K^{\cdot} tr(\Delta\boldsymbol{\epsilon}_{n+1})\mathbf{I} + 2G^{\cdot} \Delta\boldsymbol{\epsilon}_{n+1}^d \tag{A.6}$$

where

$$\boldsymbol{\sigma}^{\cdot} = p_n^h \mathbf{I} - \beta^{\cdot} \Delta T_{n+1} \mathbf{I} + \sum_{i=1}^{m} e^{-\Delta\xi_{n+1}/\theta_i} \boldsymbol{\sigma}_{t_n}^{d,} \quad \text{(A.7)}$$

$$K^{\cdot} = \frac{1}{\Delta t_{n+1}} \int_{t_n}^{t_{n+1}} \frac{1}{\kappa}\, d\tau, \quad \text{(A.8)}$$

$$G^{\cdot} = \frac{1}{\Delta t_{n+1}} \sum_{i=1}^{m} \int_{t_n}^{t_{n+1}} G_i e^{-(\xi_{n+1}-\xi(\tau))/\theta_i}\, d\tau, \quad \text{(A.9)}$$

$$\beta^{\cdot} = \frac{1}{\Delta t_{n+1}} \int_{t_n}^{t_{n+1}} \frac{\alpha}{\kappa}\, d\tau. \quad \text{(A.10)}$$

The quantities $\boldsymbol{\sigma}$, K$^{\cdot}$, G$^{\cdot}$ and $\beta^{\cdot}$ can be evaluated when the state at t_n is determined and the temperature and strain histories are known up until t_{n+1}.

Writing *Eq A.6* out into the components with respect to a local base and eliminating the incremental strain component $\Delta\epsilon_{zz}$ by means of

$$\Delta\epsilon_{zz} = \frac{\sigma_{zz} - \sigma_{zz}^{\cdot}}{a} \quad \text{(A.11)}$$

yields the following matrix-vector equation

$$\underset{\sim}{\sigma}_{n+1} = \underline{\underline{M}}\,\underset{\sim}{\Delta\epsilon} + \underset{\sim}{g} \quad \text{(A.12)}$$

with:

$$\underset{\sim}{\sigma} = [\sigma_{xx}\ \sigma_{yy}\ \sigma_{xy}\ \sigma_{yz}\ \sigma_{xz}]^T, \quad \text{(A.13)}$$

$$\underset{\sim}{\Delta\epsilon} = [\Delta\epsilon_{xx}\ \Delta\epsilon_{yy}\ \Delta\epsilon_{xy}\ \Delta\epsilon_{yz}\ \Delta\epsilon_{xz}]^T, \quad \text{(A.14)}$$

$$\underline{\underline{M}} = \begin{bmatrix} a^{\cdot} & b^{\cdot} & 0 & 0 & 0 \\ b^{\cdot} & a^{\cdot} & 0 & 0 & 0 \\ 0 & 0 & G^{\cdot} & 0 & 0 \\ 0 & 0 & 0 & G^{\cdot} & 0 \\ 0 & 0 & 0 & 0 & G^{\cdot} \end{bmatrix}, \quad \text{(A.15)}$$

$$\underset{\sim}{g} = \begin{bmatrix} \sigma_{xx}^{\cdot} + \dfrac{b}{a}(\sigma_{zz} - \sigma_{zz}^{\cdot}) \\ \sigma_{yy}^{\cdot} + \dfrac{b}{a}(\sigma_{zz} - \sigma_{zz}^{\cdot}) \\ \sigma_{xy}^{\cdot} \\ \sigma_{yx}^{\cdot} \\ \sigma_{xz}^{\cdot} \end{bmatrix}, \quad \text{(A.16)}$$

$$a = \frac{3K^{\cdot} + 4G^{\cdot}}{3}, \quad b = \frac{3K^{\cdot} - 2G^{\cdot}}{3},$$

$$a^{\cdot} = a - \frac{b^2}{a}, \quad b^{\cdot} = b - \frac{b^2}{a} \quad \text{(A.17)}$$

APPENDIX B: PARAMETERS USED IN THE CALCULATIONS

Viscosity

The viscosity is modeled using a 7-constant Cross model:

$$\eta(\dot{\gamma}, T, p) = \frac{\eta_0}{1 + (\eta_0 \dot{\gamma}/\tau^*)^{(1-n)}} \quad \text{(B.1)}$$

$$\eta_0 = H \exp\left(\frac{-c_1(T - T^*)}{c_2^{\cdot} + T - T^*}\right) \quad \text{(B.2)}$$

$$T^* = T_0 + sp \quad \text{(B.3)}$$

$$c_2^{\cdot} = c_2 + sp. \quad \text{(B.4)}$$

The parameters for this model are listed in *Table 2* for both materials.

pvT - Data

The pvT-behavior of both materials is modeled using the Tait equation.

$$T_g = T_{g0} + sp \quad \text{(B.5)}$$

$$B_m = B_{0m} e^{-B_{1m}T} \quad \text{(B.6)}$$

$$B_s = B_{0s} e^{-B_{1s}T} \quad \text{(B.7)}$$

$$v(p, T) = \begin{cases} (a_{0s} + a_{1s}(T - T_g))\left(1 - 0.0894 \ln\left(1 + \dfrac{p}{B_s}\right)\right) & (T \le T_g) \\ (a_{0m} + a_{1m}(T - T_g))\left(1 - 0.0894 \ln\left(1 + \dfrac{p}{B_m}\right)\right) & (T > T_g) \end{cases} \quad \text{(B.8)}$$

where the subscripts m, s refer to the melt and the solid phase, respectively. The data of the ABS is measured on a different material: ABS Novodur PH-AT from Bayer (20). The parameters are listed in *Table 3*.

Thermal Properties

The specific heat capacity c_p is taken constant in the melt and in the solid phase. For both materials the values are: $c_p = 2289$ J/(kgK) for $T > T_g$ and $c_p = 1785$ J/(kgK) for $T \le T_g$.

The thermal conductivity is constant in both the melt and in the solid phase. For the two materials $\lambda = 0.16$ W/(mK).

Table 2. Parameters in 7-Constant Cross Model.

		PS	ABS
n		0.2520	0.2030
τ^*	Pa	$3.080 \cdot 10^4$	$1.175 \cdot 10^5$
H	Pas	$4.76 \cdot 10^{10}$	$1.669 \cdot 10^5$
T_0	K	373	443
c_1		25.74	13.15
c_2	K	61.06	117.0
s	K/Pa	$5.1 \cdot 10^{-7}$	0

Table 3. Parameters in Tait Equation.

		PS		ABS	
		melt	glass	melt	glass
a_0	m^3/kg	$9.72 \cdot 10^{-4}$	$9.72 \cdot 10^{-4}$	$9.73 \cdot 10^{-4}$	$9.73 \cdot 10^{-4}$
a_1	$m^3/(kgK)$	$5.44 \cdot 10^{-7}$	$2.24 \cdot 10^{-7}$	$5.60 \cdot 10^{-7}$	$2.27 \cdot 10^{-7}$
B_0	Pa	$2.53 \cdot 10^{8}$	$3.53 \cdot 10^{8}$	$2.61 \cdot 10^{8}$	$3.05 \cdot 10^{8}$
B_1	K^{-1}	$4.08 \cdot 10^{-3}$	$3.00 \cdot 10^{-3}$	$3.90 \cdot 10^{-3}$	$4.10 \cdot 10^{-3}$
$T_g(0)$	K	373		363	
s	K/Pa	$5.1 \cdot 10^{-7}$		$1.47 \cdot 10^{-7}$	

Parameters Thermal Stress Calculations

For the thermal stress calculations with the viscoelastic model, a relaxation spectrum is fitted on measured data of G' and G''. The mastercurve at $T = T_r$ is constructed by shifting the measured storage and loss moduli at temperatures below T_g over the frequency axis. The master curve represents the shear modulus in the solid, since the modulus in the melt (which is nearly 1000 times less) does not contribute significantly to the stress development. For both materials, a 6-mode relaxation spectrum is used. The relaxation data are listed in *Table 4.*

When the thermo-viscoelastic model is applied, additional data are needed for the time-temperature superposition principle. To shift the relaxation data to the appropriate temperature, the WLF-shift

$$a_T(T) = 10^{\,c_1(T-T_r)/(c_2+T-T_r)} \qquad \text{(B.9)}$$

is used for $T \geq T_g$ and

$$a_T(T) = e^{-c_3(T-T_r)} \qquad \text{(B.10)}$$

for $T < T_g$. The parameters can be found in *Table 5.*

The elastic shear modulus for applying the viscous-elastic model is G_{el} = 906 M Pa for PS and G_{el} = 1012 M Pa for ABS.

Mold Properties

In the calculations, a Biot boundary condition with a (high) heat transfer coefficient of 3000 $J/(m^2sK)$ is used. The reference temperature for PS was 328 K on both mold walls. For ABS, the cooling was asymmetric with a temperature of 325 K on one mold wall and 321 K on the other. These latter conditions correspond to temperatures measured close to the mold wall.

Table 4. Relaxation Data Thermal Stress Calculations.

	PS		ABS	
i	θ_i (s)	G_i (Pa)	θ_i (s)	G_i (Pa)
1	$4.769 \cdot 10^{-8}$	$6.919 \cdot 10^{7}$	$4.706 \cdot 10^{-9}$	$5.074 \cdot 10^{7}$
2	$2.498 \cdot 10^{-6}$	$5.958 \cdot 10^{7}$	$4.410 \cdot 10^{-6}$	$8.688 \cdot 10^{7}$
3	$1.178 \cdot 10^{-4}$	$1.203 \cdot 10^{8}$	$2.082 \cdot 10^{-3}$	$2.904 \cdot 10^{8}$
4	$6.660 \cdot 10^{-3}$	$2.220 \cdot 10^{8}$	$6.198 \cdot 10^{-1}$	$4.091 \cdot 10^{8}$
5	$3.000 \cdot 10^{-1}$	$3.433 \cdot 10^{8}$	$3.035 \cdot 10^{6}$	$3.573 \cdot 10^{5}$
6	$4.496 \cdot 10^{0}$	$9.136 \cdot 10^{7}$	$2.749 \cdot 10^{8}$	$1.185 \cdot 10^{5}$

Table 5. Parameters Time-Temperature Shift Functions.

		PS	ABS
c_1		13.37	14.22
c_2	K	51.06	47.01
c_3	K^{-1}	0.6242	0.3291
T_r	K	363	373

The elasticity of the molds is given by the compliance $C_m = 2.3 \cdot 10^{-13}$ $m^3/(Ns)$ for specimen A (PS) (3) and $C_m = 6.0 \cdot 10^{-13}$ $m^3/(Ns)$ for specimen B (ABS).

ACKNOWLEDGMENTS

The first author is grateful to Mr. L. Fokke from University of Twente for assistance with the layer removal experiments and also to the Domestic Appliances and Personal Care Division of Philips for the opportunity of carrying out the experimental part of this research.

Stimulating discussions with L. C. E. Struik and F. P. T. Baaijens are gratefully acknowledged.

REFERENCES

1. F. P. T. Baaijens, *Rheol. Acta,* **30,** 284 (1991).
2. L. F. A. Douven, PhD thesis, Eindhoven University of Technology, The Netherlands (1991).
3. A. A. M. Flaman, PhD thesis, Eindhoven University of Technology, The Netherlands (1990).
4. L. F. A. Douven, F. P. T. Baaijens, and H. E. H. Meijer, *Prog. Polym. Sci.,* **20,** 403 (1995).
5. A. I. Isayev and C. A. Hieber, *Rheol. Acta.,* **19,** 168 (1980).
6. R. Wimberger-Friedl, PhD thesis, Eindhoven University of Technology, The Netherlands (1991).
7. H. Janeschitz-Kriegl, *Rheol. Acta,* **16,** 327 (1977).
8. G. Titomanlio, V. Brucato, and M. R. Kamal, *Int. Polym. Proc.,* **1,** 55 (1987).
9. L. C. E. Struik, *Polym. Eng. Sci.,* **18,** 799 (1978).
10. L. C. E. Struik, *Internal Stresses, Dimensional Instabilities and Molecular Orientations in Plastics,* John Wiley & Sons, New York (1990).
11. R. Wimberger-Friedl and R. D. H. M. Hendriks, *Polymer,* **30,** 1143 (1989).
12. W. T. Read, Jr., and R. G. Treuting, *J. Appl. Phys.,* **2,** 130 (1951).
13. A. I. Isayev, ed., *Injection and Compression Molding Fundamentals,* Marcel Dekker Inc., New York (1987).
14. C. L. Tucker III, *Fundamentals of Computer Modeling for Polymer Processing,* Hanser Publishers, Munich (1991).
15. J. D. Ferry, *Viscoelastic Properties of Polymers,* 3rd Ed., John Wiley & Sons, New York (1980).
16. T. J. R. Hughes, *The Finite Element Method,* Prentice-Hall International Inc. (1987).
17. E. N. Dvorkin and K. J. Bathe, *Eng. Comput.,* **1,** 77 (1984).
18. K. J. Bathe and E. N. Dvorkin, *Int. J. Num. Meth. Eng.,* **21,** 367 (1984).
19. C. H. V. Hastenberg, P. C. Wildervanck, A. J. H. Leenen, and G. G. J. Schennink, *Polym. Eng. Sci,* **32,** 506 (1992).
20. VDMA, *Kenndaten für die Verarbeitung thermoplastischer Kunststoffe,* Volume 1, Thermodynamik, Carl Hanser Verlag, Munich (1979).

Revision received July 1995